Available online at www.keaipublishing.com/en/journals/journal-of-magnesium-and-alloys/

ScienceDirect

Journal of Magnesium and Alloys 13 (2025) 3689–3701

www.elsevier.com/locate/jma

Full Length Article

A multi-level biomimetic LDH coatings with super hydrophobicity, corrosion resistance, anti-icing and anti-fouling properties on magnesium alloy[☆]

Lin Dai, Hongzhi Cui[*], Xiaohua Chen, Ruiqi Xu, Yuhao Zhang, Leigang Li

College of Materials Science and Engineering, Ocean University of China, Qingdao, 266100, China

Received 31 December 2024; received in revised form 19 March 2025; accepted 21 April 2025
Available online 13 May 2025

Abstract

In this study, femtosecond pulsed laser processing was applied to the magnesium alloy, followed by in situ growth of Mg-Al layered double hydroxides (LDHs), and finally modification with low surface energy materials to prepare a biomimetic of centipede-like superhydrophobic composite coating. The resulting biomimetic coating features a dual-scale structure, comprising a micron-scale laser-etched array and nano-scale LDH sheets, which together create a complex hierarchical architecture. The multistage bionic superhydrophobic coating exhibits exceptional corrosion resistance, with a reduction in corrosion current density by approximately five orders of magnitude compared to the bare magnesium alloy substrate. This remarkable corrosion resistance is attributed to the synergistic effects of the superhydrophobicity with a contact angle (CA) of 154.60°, the densification of the surface LDH nanosheets, and the NO$_3^-$ exchange capacity. Additionally, compared to untreated AZ91D alloy, the biomimetic coating prolongs ice formation time by 250% at -40 °C and withstands multiple cycles of sandpaper abrasion and repeated tape peeling tests. Furthermore, it demonstrates excellent self-cleaning and anti-fouling properties, as confirmed by dye immersion and dust contamination tests. The construction of the multi-level bionic structured coating not only holds significant practical potential for metal protection but also provides valuable insights into the application of formed LDH materials in functional bionic coating engineering.

Keywords: LDH coatings; Bionic structure; Super hydrophobicity; Corrosion resistance; Anti-Icing and Anti-Fouling.

---

1. Introduction

The rapid development of marine equipment puts forward higher and higher requirements for lightweight materials and materials adapted to extreme environments. Magnesium (Mg) alloys exhibit several desirable properties, including low density, high specific strength, excellent biocompatibility, and effective electromagnetic shielding [1]. These characteristics make them promising metal structural materials for a range of applications in the automotive industry, biomedicine, aerospace, and electronics [2,3]. With the implementation of maritime power strategies, the marine atmospheric environment has become one of the key service environments for advanced Mg alloy materials and their structural components [4]. However, Mg alloys are highly reactive, forming an unstable Mg(OH)$_2$ layer when exposed to water, which compromises their corrosion resistance and limits their use in demanding conditions [5,6]. Addressing this corrosion issue is critical to expanding the applications of Mg alloys, particularly in marine and other extreme environments [7].

Up to now, various approaches have been employed to enhance the corrosion resistance of Mg alloys, mainly encompassing two categories: metallurgical methods and surface protection techniques. The first category of metallurgical methods usually bases on purification of Mg alloys [8], homogenization of microstructure and composition, and alloying, etc. [6]. Nevertheless, these approaches demonstrate limited success in the prevention of galvanic corrosion [9].

[☆] Peer review under the responsibility of Chongqing University.

[*] Corresponding author.

E-mail address: cuihongzhi@ouc.edu.cn (H. Cui).

https://doi.org/10.1016/j.jma.2025.04.012

While the second category generally refers to surface protection techniques, including electroplating, spraying [10], chemical conversion coatings [11], micro-arc oxidation [12,13], etc. These methods, however, need to be complemented with anti-fouling and anti-icing capabilities to meet the specific demands of marine and extreme environments [14].

Superhydrophobic modification offers a promising solution to overcome these limitations by combining corrosion protection with other functional characteristics. The properties of superhydrophobic materials have been the subject of considerable research in recent years, particularly in the context of biomimetic surface structures [15]. The fabrication of superhydrophobic coatings on magnesium alloy surfaces can effectively isolate corrosive media from the metal substrate, thereby significantly enhancing the protective performance of the magnesium alloy [16]. Furthermore, such superhydrophobic surfaces can endow magnesium alloys with multifunctional properties, including self-cleaning [17,18], antimicrobial properties [19], anti-icing capabilities [20,21], drag reduction [22,23], and enhanced mechanical robustness [24]. Pulsed laser processing offers diversified merits such as high efficiency, simplicity, precision, and versatility, making it suitable for the fabrication of complex micro- and nanostructures [25,26]. Jiang et al. [27] developed a novel superhydrophobic F-L@KHSiO$_2$/OTMS coating through femtosecond laser etching, spraying, and chemical modification. This coating exhibited excellent superhydrophobic properties, with a contact angle of 165.92° and an ice delay time of 730 s at −20 °C, highlighting its potential for applications in efficient anti-icing, deicing, and defrosting. Zhou et al. [28] employed laser techniques to construct biomimetic honeycomb and micropillar arrays, enabling the bionic surface to achieve high-efficiency anti-icing and deicing under low-temperature conditions. The bionic surface maintained superior ice-delay performance at -15 °C, while resisting severe mechanical damage from abrasive objects. Pan et al. [29] fabricated a tri-scale superhydrophobic surface using laser processing. The surface consisted of periodic micro-cone arrays, densely grown nanograss, and scattered microflowers. After 10 cycles of icing and deicing tests, the surface's ice adhesion strength remained below 10 kPa. Feng et al. [30] utilized ultrafast laser processing to create a bamboo leaf-inspired surface on a copper substrate. The surface was composed of periodic micropapillae and microbridge arrays with compact nanoclusters (MLMN) in between. The freezing time of a 15 µL drop of distilled water on the surface was extended to 921 s, and freezing of 35% saline solution was delayed to 1110 s.

In recent years, LDHs coatings are favored in the field of corrosion protection for Mg alloys due to their easily tunable composition and adaptable structure [31]. Particularly when LDHs are applied as a film layer on the surface of the protected object, the resulting dense, uniform, and stable LDHs film can serve as a physical barrier, effectively isolating the corrosive media from direct contact with the protected object [32]. However, the porous nature of LDH coatings allows for the penetration of corrosive agents, compromising their protective efficacy [33,34]. To extend the service life of LDHs coatings, it is imperative that additional protective coatings be employed to seal the pores of LDHs surfaces. The in-situ prepared LDHs coating can effectively protect the metal substrate [35]. The bifunctional composite superhydrophobic anti-corrosion coating consists of a surface layer of LDH powder, a middle layer of Polydimethylsiloxane, and a bottom layer of in-situ grown LDH film. The static contact angle of the composite SHB coating is 155°. This coating significantly reduced the corrosion current density (I_{corr}) to 6.447×10^{-9} $A \cdot cm^2$ [36]. Pillado et al. [37] synthesized various Zn-Al and Li-Al LDH systems containing Li-, Mo-, and W-based corrosion inhibitors. Among these LDHs, the Zn-Al LDH W and Li-Al LDH Li exhibited the highest corrosion resistance, providing new insights into enhancing the corrosion resistance of LDHs. Among the numerous varieties of LDHs, the direct preparation of Mg-Al LDHs on Mg alloys offers notable advantages [38]. The Mg-Al LDHs film layer contains elements that are common to the Mg alloy matrix, which facilitates the formation of dense Mg-Al LDHs nanosheets on the alloy surface. Wang et al. [16] in situ grew Mg-Al LDH corrosion inhibitors on the surface of AZ31 Mg alloy and subsequently sealed them with a superhydrophobic coating, resulting in an effective anti-corrosion coating. The synergistic effect of molybdates and lauric acid contributed to the improved corrosion resistance of the coating. The water repellent properties of superhydrophobic surfaces indicate considerable potential for the protection of metals from corrosion [39]. The construction of superhydrophobic coatings on the surface of LDHs can enhance its corrosion protection, and by utilizing the corrosion resistance properties of superhydrophobic surfaces, a dual protective composite coating can be formed on the Mg alloy surface [14]. Under superhydrophobic conditions, binary hierarchies that combine both scales perform better in most cases.

In this study, inspired by the self-cleaning properties of micro and nano-structure surface of centipede body, a multi-stage bionic superhydrophobic composite coating based on AZ91D magnesium alloy was constructed by femtosecond pulsed laser processing, in-situ growth and low surface energy material modification. The surface micron-level topography can be adjusted by changing the etching process parameters, to obtain different hydrophobic properties and achieve controllable preparation of surfaces with different wetting states. The resulting bionic coating exhibits excellent corrosion resistance, self-cleaning, anti-icing, and anti-fouling performance, offering a promising solution for enhancing the longevity and functionality of Mg alloys in marine and extreme environmental applications.

2. Experimental procedures

2.1. Materials

Commercial casting AZ91D Mg alloy was purchased from Dongguan Kuangyu Metal Co., LTD. $Al(NO_3)_3 \cdot 9H_2O$ (>99.5%), NaOH (>99.5%), 1H, 1H, 2H, 2H-Tridecafluoro-n-octyltriethoxysilane (PFOTES) were all purchased from

Shanghai Macklin Biochemical Technology Co., Ltd. $NaNO_3$ was obtained from China National Pharmaceutical Group Chemical Reagent Co., Ltd. Deionized water acted as solvent in this study.

2.2. Experimental methods

2.2.1. Femtosecond laser primary structure design

The AZ91D substrate was initially polished using 800 #, 1200 #, and 1500 # silicon carbide papers to remove contaminants and the natural oxide layer. The samples were then subjected to ultrasonic cleaning in alcohol and deionized water, followed by rapid air-drying at 20 °C room temperature using the cool air setting of a blow dryer. Femtosecond laser processing was performed using a laser with a central wavelength of 1030 nm, pulse width of 350 fs, and repetition rate of 400 kHz. On the polished surface, the scanning speed was set to 1000 mm/s with a pump current of 80% (corresponding to an output power of 1.2 W). Cross-line scanning was carried out with different line spacings of 20, 30, and 40 µm at 90 angles. All laser processing was performed in an argon atmosphere to minimize secondary oxidation, reduce magnesium combustion risk, and control sparking and spattering during treatment. After laser treatment, the samples were ultrasonically cleaned in deionized water for 10 min for further use (denoted as “Laser”). This process resulted in the formation of a primary biomimetic structure.

2.2.2. In situ growth of LDH secondary structure

The $Al(NO_3)_3{\cdot}9H_2O$ (0.02 mol) and $NaNO_3$ (0.01 mol) were continuously stirred and dissolved in deionized water. The solution was magnetically stirred, and the pH was adjusted to 11 by gradually adding 4.0 M NaOH solution. The laser-etched samples were then vertically placed in a stainless steel autoclave containing the mixed solution and subjected to hydrothermal treatment at 120 °C for 14 hours to promote the in situ synthesis of the Mg-Al LDH coating. Subsequently, the samples were washed with deionized water and dried (denoted as “LMAL”).

2.2.3. Preparation of superhydrophobic surface of bionic structure

LMAL was soaked in an alcohol solution of 1.0 vol.% PFOTES for 2 h, and then dried in an oven at 120 °C for 2 h (denoted as “LMALP”).

2.3. Characterization

An X-ray diffractometer (XRD, Bruker D8 ADVANCE, scanning at 4°/min) was used to characterize the phase composition of the samples with a Cu K_α radiation source. The chemical structures were characterized by Fourier transformation infrared spectrometry (FT-IR, Thermo Scientific Nicolet iS5, USA, 400–4000 cm^{-1}). The microscopic morphology of the samples was observed on a ZEISS-Gemini SEM300 field emission scanning electron microscope. The element distribution was analyzed using the attached energy dispersive spectrometer (EDS) spectrometer. Confocal laser scanning microscope (CLSM, VK-X250) used to observe the surface roughness. X-ray photoelectron spectroscopy (XPS, Thermo Scientific K-Alpha) recorded the surface chemical composition of the prepared samples. The static water contact angle (WCA) of the superhydrophobic coating was measured by a contact angle measuring instrument (datphysics OCA25, Germany).

2.4. Performance of coating

Sandpaper wear method (100 g weight, 1500 # SiC sandpaper) was used to evaluate the mechanical wear resistance of the coating. The coating was placed in a refrigerator at -40 °C, then an equal amount of deionized water was added, and the camera captured footage of the liquid freezing. To investigate the corrosion resistance of different samples in 3.5 wt.% NaCl solution, Tafel polarization curves and electrochemical impedance spectroscopy (EIS) were measured in a three-electrode system using the Gamry electrochemical workstation (Gamry Reference 600+, USA) with Framework^{TM} software version 7.8.2.7430. A conventional three-electrode system (exposed area of different coated samples is 1 cm^2, actual test area is 1 cm^2, saturated calomel electrode (SCE, 0.242 V vs standard hydrogen electrode) as the reference electrode, platinum sheet (20 mm × 20 mm) as the reverse electrode) was used to monitor the corrosion resistance of the composite coating. The samples were immersed in 3.5 wt.% NaCl solution for 30 min and then tested by electrochemical impedance spectroscopy (EIS) with a frequency range of 10^{-2}–10^5 Hz and an AC voltage of 20 mV. All EIS measurements were performed three times to ensure repeatability. The obtained impedance data were analyzed using Gamry Echem Analyst software with appropriate equivalent circuit modeling. The Tafel polarization curve was measured at a scan rate of 2 mV/s at ±250 mV open circuit potential (OCP). Corrosion potential and corrosion current are extrapolated from the cathode and anode regions of the Tafel diagram.

3. Results and discussion

3.1. Structure characterization

The XRD patterns of different film layers are shown in Fig. 2a. After laser treatment, the peak strength of Mg showed a significant increase trend, which may be attributed to the change of the preferred orientation plane in AZ91D after laser processing due to the higher solidification rate, grain refinement and nanostructure formation [40], the XRD diffraction peak of Mg is sharper. The typical crystal-plane diffraction peaks of LMAL appear at 11.5° and 23.2°, corresponding to the (003) and (006) planes [41], respectively. This result is consistent with the published values for LDH coatings, indicating that the LDH was successfully synthesized on the Mg alloy surface after laser treatment. Additional characteristic

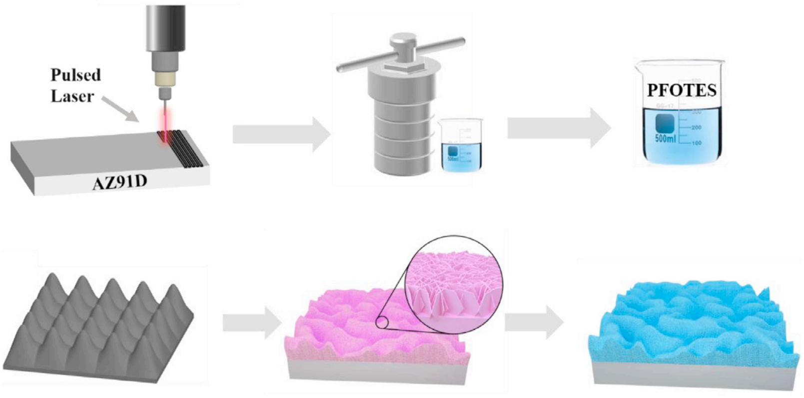

Fig. 1. Schematic diagram of the preparation of the LMALP film layer.

peaks at 18.5°, 38.1°, 58.7°, and 62.0° correspond to the by-product $Mg(OH)_2$, which is formed through the in-situ growth of LDH. After deposition of LDH, part of the Mg diffraction peak is attenuated, and part of the Mg signal is shielded by the orientation of the LDH sheets.

The FT-IR spectra of Laser, LMAL, and LMALP are shown in the Fig. 2b. The absorption peaks at 3686 cm^{-1} and 3430 cm^{-1} are attributed to the stretching vibrations of H–O–H and the symmetric contraction of O–H, respectively. The absorption peak observed at 1599 cm^{-1} corresponds to the bending vibration of water molecules, indicating the presence of absorbed water and interlayer water on the coating surface. An absorption peak at 1358 cm^{-1}, observed in the LMAL spectrum, is attributed to the stretching vibration of NO_3^- within the LDH interlayer, confirming the successful synthesis of Mg-Al LDH [42]. In the 2600–3000 cm^{-1} range, weaker peaks are observed, prompting an expansion of this range to acquire more detailed data. For LMALP, absorption peaks at 2980 cm^{-1} and 2925 cm^{-1} are assigned to the asymmetric and symmetric stretching vibrations of -CH_2, while peaks at 1087 cm^{-1} and 1189 cm^{-1} are attributed to the Si-O and C-F bonds [43]. These observations confirm the successful modification of the LDH surface with PFOTES.

Fig. 3 shows the scanning electron microscope (SEM) images of Laser with laser-controlled scan line spacing of 20 µm and LMALP. After laser treatment, the surface of the Mg matrix is replaced by regular micron-scale columnar structures (Fig. 3a). The high-power morphology of the columnar structure is shown in Fig. 3a_1 and a_2, where some protrusions and deep pits can be seen on the surface. Fig. 3b and b_1 shows the morphology of LMALP. It can be seen that the surface of the substrate after laser treatment has been successfully covered by a dense LDH film layer. A large number of LDH nanosheets can be seen in Fig. 3b_2, and the pits have been filled with LDH sheets, forming a more complex and compact surface micron/nanometer scale structure, which is very important for the super hydrophobic properties.

Fig. 4a shows the SEM and EDS images of LMALP. It can be seen that Mg and Al are enriched on the surface of LDH, and the appearance of a large number of O elements is mainly due to the formation of LDH and fluorosilane films. The formed LDH not only fills the deep pits, but also prevents the direct contact between the substrate and the corrosive medium, which plays an important protective role for the Mg alloy. The appearance of C, Si and F elements also demonstrates the successful formation of fluorosilane films on the surface. Fig. 4b-d shows the 3D roughness distribution of different samples under laser confocal microscopy. Due to femtosecond laser etching, the surface roughness of the laser is 3.715 µm, forming a micro-island structure. In addition, the surface roughness of LMAL and LMALP is as high as 4.238 µm and 4.347 µm, respectively, indicating that the LDH nanosheets grown on Mg matrix by hydrothermal reaction contribute to the improvement of roughness.

Due to the arbitrary orientation of nanosheets growing on the Mg alloy substrate, only cross-sections of hexagonal nanosheets were observed in Fig. 5a. The TEM analysis further revealed that Mg-Al LDH formed in situ on the surface of the magnesium alloy. EDS analysis shows that the LDH nanosheets are predominantly composed of Mg, Al, N, and O elements (Fig. 5b), which is consistent with the expected composition of Mg-Al LDH. Furthermore, the distribution of F and Si elements on the surface of the nanosheets, as indicated by the EDS mappings, confirms the successful modification of the LDH surface with PFOTES.

The composition of Laser, LMAL, and LMALP was measured by XPS, with the measurement spectra shown in Fig. 6a. Compared to Laser, the N 1s signal originates from the in situ grown LDH coating. The Si 2p and F 1s signs are attributed to PFOTES. The high-resolution C 1s spectrum of LMALP exhibits two prominent peaks at 291.78 eV and 294.11 eV (Fig. 6b), corresponding to the C-F_2 and C-F_3 groups, respectively. Additionally, peaks at 285.28 eV and 284.38 eV are attributed to the C–O and C–C bonds. The N 1s peaks, observed 400.48 eV, is attributed to the N–O bonds in the LDH (Fig. 6c). The Si 2p peaks (Fig. 6d), detected at 102.16 eV, corresponds to the Si-O bonds in PFOTES [38]. The F 1s peak in Fig. 6e, observed at 689.06 eV, is assigned to the F-C bonds in PFOTES, in agreement with the interpretation of the C 1s peaks in Fig. 6b. These results confirm the successful modification of the low surface energy material on the surface of the biomimetic structure.

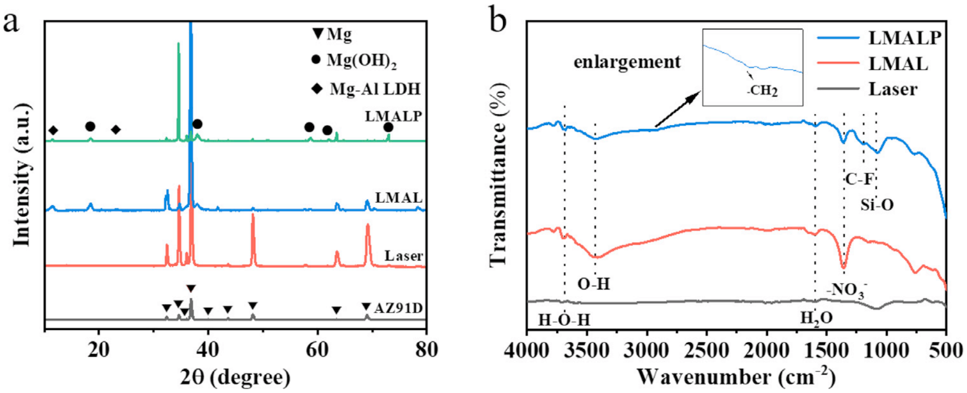

Fig. 2. (a) XRD spectra and (b) FT-IR diagram of different samples.

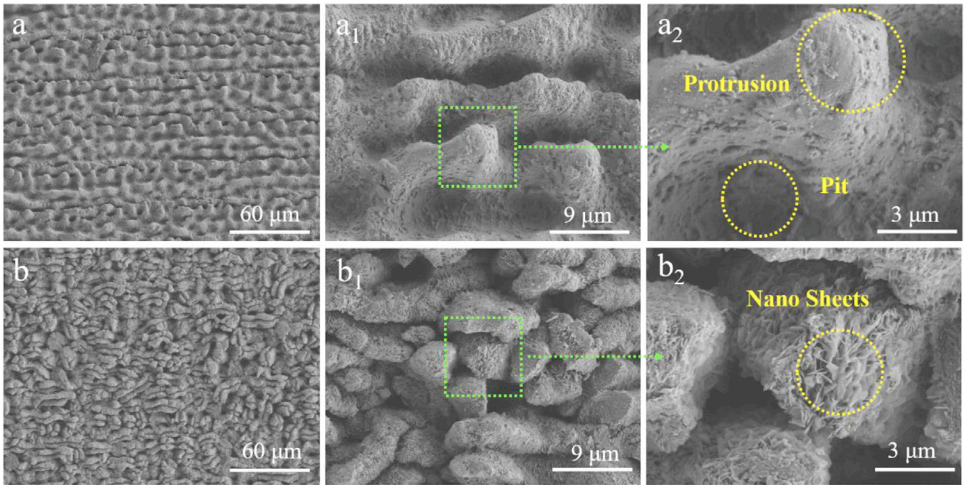

Fig. 3. SEM images of (a-a_2) Laser, and (b-b_2) LMALP.

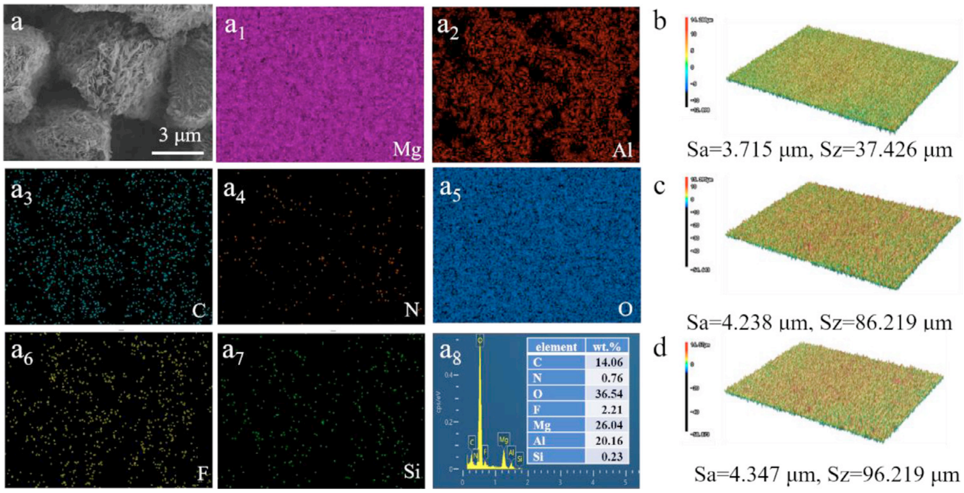

element	wt.%
C	14.06
N	0.76
O	36.54
F	2.21
Mg	26.04
Al	20.16
Si	0.23

Fig. 4. (a) SEM and (a_1-a_8) EDS spectra of LMALP. The surface morphology and roughness of (b) Laser, (c) LMAL and (d) LMALP measured by CLSM.

3.2. Evaluation of wettability

The wettability of the material mainly depends on its surface microstructure and surface chemical composition. The surface wettability of different coatings is evaluated by WCA test, as shown in Fig. 7. The contact angles of LMAL and LMALP in the primary structure are given when the femtosecond laser scanning line spacing is 20 µm, 30 µm and 40 µm (Fig. 7a-f), respectively. The contact angle of LMALP film layer with 20 µm thickness is the largest, indicating that the

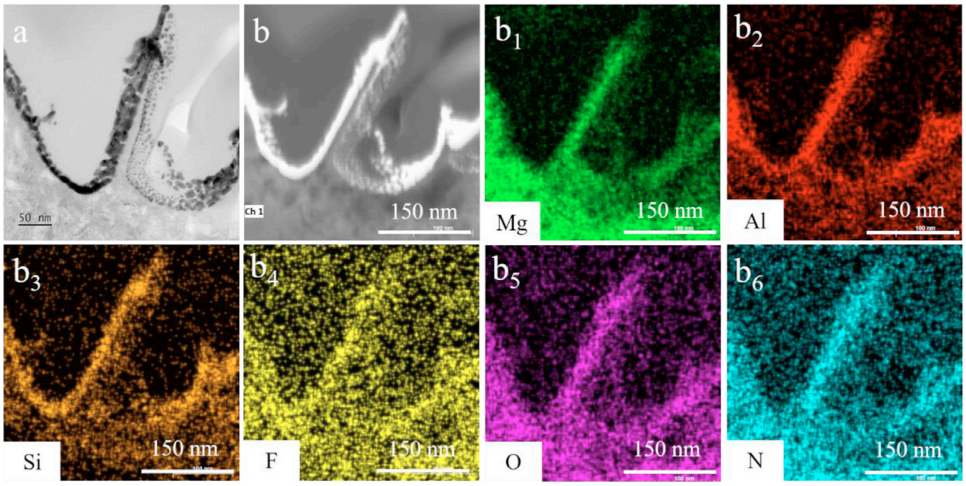

Fig. 5. (a) TEM image and (b-b_6) EDS mappings of LMALP.

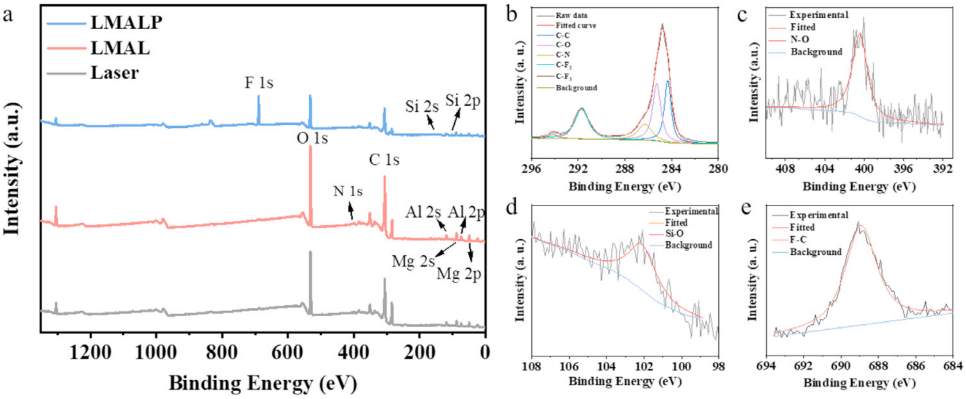

Fig. 6. XPS survey spectra of (a) Laser, LMAL and LMALP. High-resolution XPS spectra and fitting results of (b) C 1s, (c) N 1s, (d) Si 2p and (e) F 1s for LAMLP.

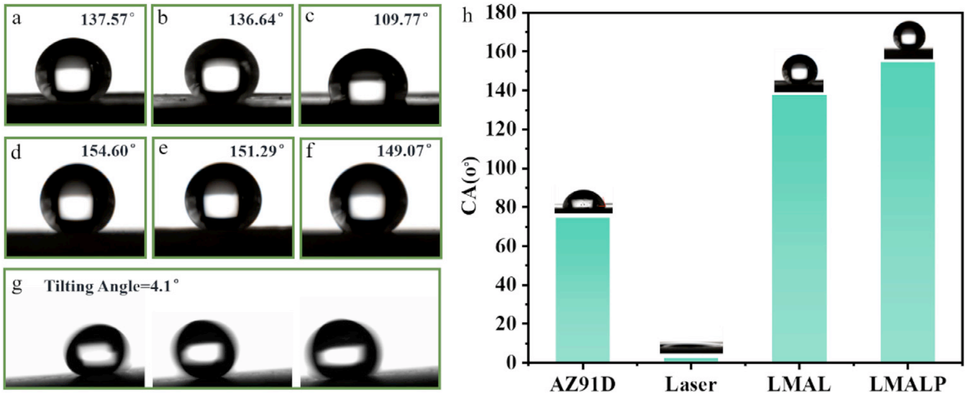

Fig. 7. WCA of LMAL with line spacing of (a) 20 µm, (b) 30 µm, and (c) 40 µm. WCA of LMALP with line spacing of (d) 20 µm, (e) 30 µm, and (f) 40 µm. (g) Rolling behavior of water droplet on LMALP. (h) WCA of different samples.

regular micro-nano convex structure after femtosecond laser processing affects the hydrophobicity of the final prepared composite film layer. In addition, the dynamic behavior of water droplets on the specimen surface was also discussed. As shown in Fig. 7g, when the tilting table is slowly tilted to 4.1°, water droplets can quickly roll off its surface, indicating that the LMALP coating has excellent hydrophobicity.

Fig. 7h presents the water contact angles of various coatings. Compared to bare magnesium alloy, the water contact angle of the Laser surface is less than 3°, indicating a transition to superhydrophilicity. This behavior arises from the high-energy femtosecond laser beam, which oxidizes the magnesium alloy surface, thereby increasing the surface energy of the newly formed material. As a result, the surface exhibits

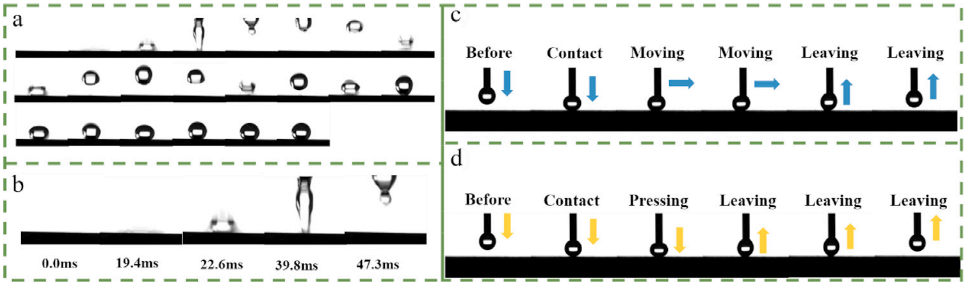

Fig. 8. (a, b) droplet bounce experiment of LMALP film layer. (c) Photos of a droplet leaving behavior after being dragged laterally and (d) squeezed longitudinally.

hydrophilic and superhydrophilic characteristics. LDH is hydrophilic, but the contact angle of the LMAL coating reaches 137.57°, indicating that the gas chamber formed by the micro-nano structure resists part of the hydrophilicity of LDH itself, making the coating hydrophobic. The LMALP film layer has a contact angle of 154.60°, and works in the same way as the lotus leaf due to its unique micro/nano layered structure and low surface energy coating. When the liquid comes into contact with a rough, super-hydrophobic surface, it is unable to fully penetrate into the surface texture, but instead forms an uneven wetted state of a composite interface consisting of solid, liquid and air. The surface energy is calculated by using the polar substance water and the non-polar substance diiodomethane according to the Owens and Winter formula [44]. The surface free energy of AZ91D is 40.38 mJ/m^2, and the surface free energy can be reduced to 7.8 mJ/m^2 after LMALP coating. The results show that LMALP coating has low surface energy and excellent superhydrophobicity.

The superhydrophobic surface can exhibit the phenomenon of small droplets bouncing due to the difficulty in converting the kinetic energy of the droplets into the internal energy of the superhydrophobic coating. Additionally, the surface tension of superhydrophobic coatings is typically low. When a droplet impacts the surface of a superhydrophobic coating at low temperatures, it bounces off the surface before ice nucleation can occur, thereby slowing down the process of supercooling transfer at the interface and effectively preventing ice formation on the surface [45]. To further investigate the dynamic process of droplet adhesion, the impact of droplets on the coating was recorded. As shown in Fig. 8a, water droplets (10 µL) released from a height of 1 cm exhibit three rebound cycles on the coating surface. The solid-liquid contact time during the first impact-rebound cycle is measured to be 27.9 ms. Fig. 8b illustrates the first droplet impact, where the droplet exhibits significant rebound after contacting the LMALP coating, fully detaching from the surface at 47.3 ms and subsequently shrinking into a pancake-like shape. This demonstrates that the LMALP coating possesses excellent water-repellent properties, making it highly suitable for applications in self-cleaning, anti-fouling, and related fields. Fig. 8c, d demonstrates the horizontal and vertical manipulation of water droplets on the superhydrophobic coating. In both scenarios, the biomimetic superhydrophobic surface leaves no residual liquid, and the droplets ultimately detach smoothly. This indicates minimal adhesion between the droplets and the coating surface, further confirming the excellent superhydrophobic properties of the biomimetic surface.

3.3. Anti-icing property

The water-repellent properties of superhydrophobic surfaces are primarily attributed to their exceptionally low contact angle hysteresis, which facilitates droplet retraction and rebound, thereby reducing surface contact time. This mechanism can be leveraged to mitigate icing by minimizing the interaction between water droplets and the substrate. To assess the anti-icing performance of the biomimetic superhydrophobic surface, static anti-icing tests were conducted on AZ91D Mg alloy and LMALP composite films at an ambient temperature of -40 °C, as illustrated in Fig. 9a and b. Initially, the droplet surface is transparent. With heat transfer progressed, the droplet began to freeze from the bottom upward. On the LMALP coating, it took approximately 59 s for the droplet's outer edges, in direct contact with the environment, to completely freeze into frost. Subsequently, the freezing front expanded inward from the frosted periphery, culminating in the formation of a fully frozen droplet at 112 s. In contrast, ice crystals formed on the bare Mg alloy within 46 s, demonstrating the superior anti-icing performance of the LMALP composite film compared to the untreated substrate.

In the process of droplet freezing, the formation rate of ice crystals is the nucleation rate of the droplet. The delayed freezing observed with LMALP coatings can be explained by thermodynamic principles.

$$J = J_O exp\left(-\Delta G K_B{}^{-1} T^{-1}\right) \tag{1}$$

Where J is the nucleation rate, J_0 is the Boltzmann constant, T is the surface temperature, ΔG is the free energy barrier of heterogeneous nuclei, which can be defined as:

$$\Delta G = \frac{16\pi \sigma_{sv}{}^{3}}{3\Delta G_{f,v}} f(\theta) \tag{2}$$

$$f(\theta) = \frac{1}{4}(2 + cos\theta)(1 - cos\theta)^2 \tag{3}$$

Where σ_{sv} is the surface energy of the solid-gas interface, $\Delta G_{f,v}$ is the difference in volume free energy between ice and

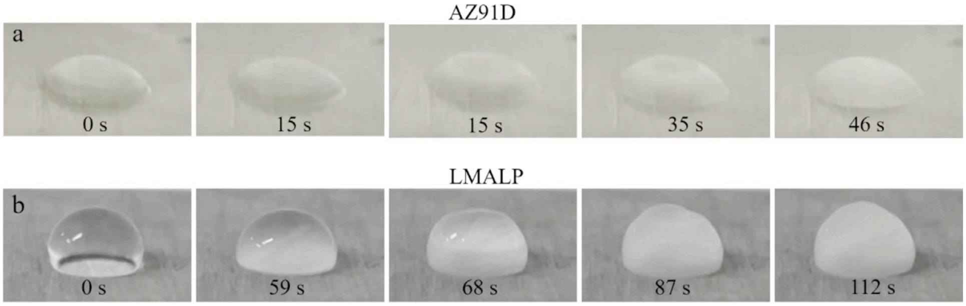

Fig. 9. Static anti-icing performance of a single droplet on (a) AZ91D and (b) LMALP.

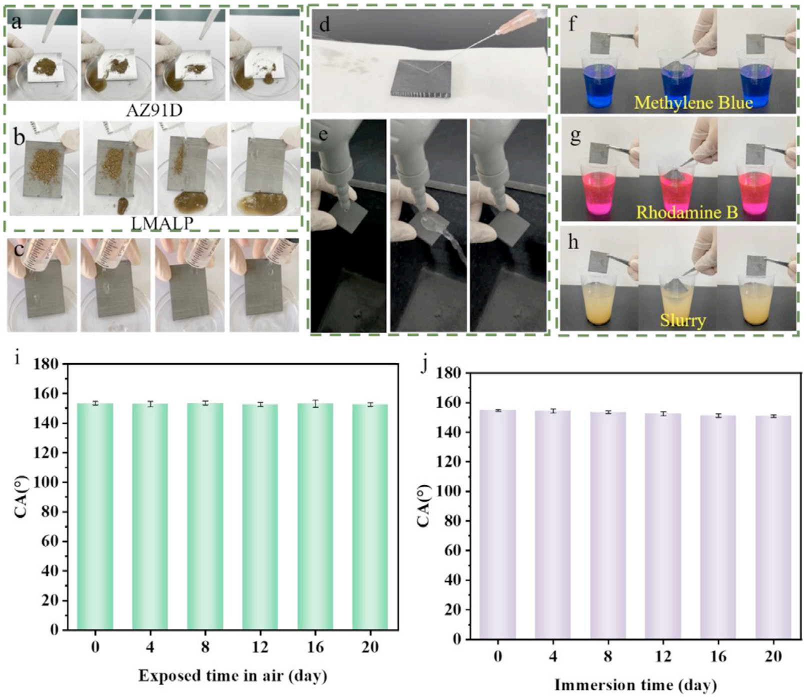

Fig. 10. (a) AZ91D, (b) LMALP antifouling performance test. (c) Self-cleaning effect, (d) water flow reflection, and (e) water flow resistance of LMALP. The appearance of the superhydrophobic surface being immersed and removed from the (f) methylene blue, (g) rhodamine B, and (h) muddy water. The contact angle of LMALP (i) exposed to air and (j) immersed in muddy water for 20 days.

liquid, and θ is the contact angle. When the θ of the LMALP coating surface is greater than 150°, the gas/solid interface of solid water droplets greatly reduces the actual contact area, delays the interfacial heat transfer, causes the value of $f(\theta)$ and ΔG to increase, reduces the nucleation rate of ice, and impedes the growth and propagation of ice crystals [46].

3.4. Self-cleaning and anti-fouling properties

As shown in Fig. 10a, for the exposed surface of AZ91D Mg, dust particles adhere a long with the water droplets, and the dust cannot be removed. On the LMALP coated surface (Fig. 10b), however, the dust is rapidly removed with the water droplets, leaving no residue behind. This effect results from the extremely low sliding angle of the superhydrophobic surface, which causes the adhesive force between the water droplets and the dust particles to be significantly higher than that between the superhydrophobic surface and the dust particles. Consequently, the water droplets effectively bind to the dust particles and remove them, keeping the surface clean. Fig. 10c illustrates the adhesion behavior of water droplets on the LMALP surface. When water droplets are dripped onto the surface, which is tilted at an angle of less than 10, the droplets do not adhere to the surface and instead roll off. In addition, the composite coating exhibits a strong ability to repel water flow. Despite the influence of high-speed water flow, the superhydrophobic surface maintains a stable Cassie-Baxter state [47], as shown in Fig. 10d and e. The storage stability of LMALP was tested by exposing it to air for 20 days. Changes in CA with storage time were detected, as shown in Fig. 10i. The results show that the CA of the superhydrophobic coating surface is greater than 153°, and the contact Angle of LMALP in the air does not change. Fig. 10j shows the CA changes of the superhydrophobic material with prolonged immersion in sewage. The results showed that CA decreased slightly with the extension of soaking time. After

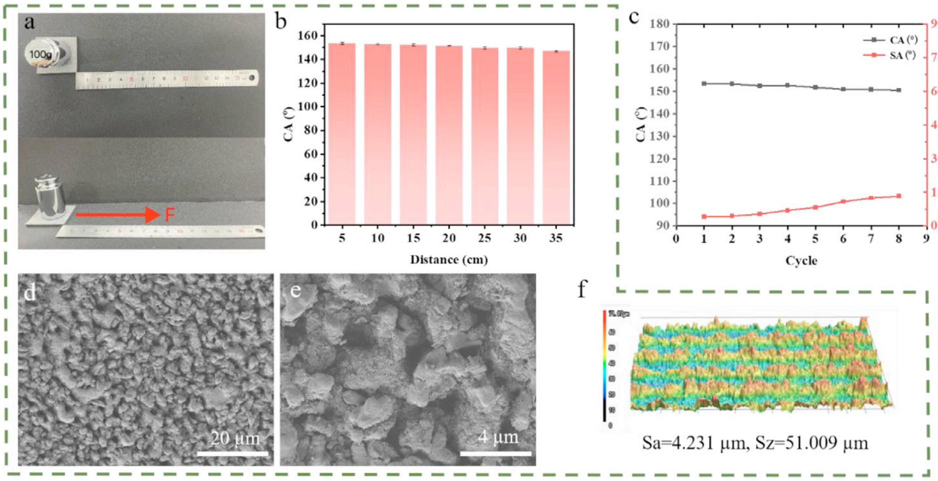

Fig. 11. (a, b) Sandpaper wear cycle test. (c) Tape stripping test. (d, e) SEM image of LMALP film layer after sandpaper wear. (f) Laser confocal image of the LMALP film layer after sandpaper wear.

soaking for 20 days, CA remained above 150°. The results showed that the prepared superhydrophobic material had excellent long-term anti-fouling ability.

To further assess the self-cleaning properties of the coating, methylene blue, rhodamine B, and slurry are selected as liquid contaminants (Fig. 10f-h). During the self-cleaning test, the LMALP samples are immersed in the various contaminants. Upon removal from the contaminated liquid, the coated films remain completely dry, showing no signs of wetting and demonstrating excellent non-wetting and anti-fouling properties.

3.5. Mechanical durability

The mechanical durability of the coating was evaluated using sandpaper abrasion and tape peeling tests. A 100 g weight was applied to the coating, with 1500 # SiC sandpaper placed underneath (Fig. 11a). Each abrasion cycle involved a sliding distance of 5 cm, repeated for a total of seven cycles. The wear resistance results shown in Fig. 11b indicate a slight decrease in the CAwith the increase in wear distance. When the accumulated wear distance exceeded 20 cm, a CA of less than 150° was observed. As shown in Fig. 11d and e, the microstructural morphology of the worn coating reveals that the LDH nanosheets on the surface were abraded, which is attributed to surface structural damage caused by friction. However, the nanosheets within the surface recesses remained intact, preserving the hydrophobicity. After sandpaper abrasion, the surface roughness (Sa) of the composite coating decreased to 4.231 μm (Fig. 11f), showing only a slight reduction compared to the unabraded composite coating. The results of the tape peeling test (Fig. 11c) exhibit a similar trend to the sandpaper abrasion test. After eight consecutive tape peeling cycles, the contact angle of the coating remained virtually unchanged, and the rolling angle increased, indicating strong adhesion between the LMALP coating and the magnesium alloy substrate. This finding demonstrates the coating's excellent mechanical durability under applied mechanical stress while maintaining its hydrophobic properties.

Table 1
Polarization curves analyses of different samples in 3.5% NaCl solution for 30 min.

Sample	E_{corr} (V/SCE)	i_{corr} (A/cm^2)
AZ91D	−1.446	0.899×10^{-3}
Laser	−1.486	0.165×10^{-3}
LMAL	−1.454	1.007×10^{-5}
LMALP	−1.319	1.695×10^{-6}

3.6. Anti-corrosion property

To assess the corrosion resistance of the coatings, the samples were initially immersed in a 3.5 wt.% NaCl solution for 30 min, followed by potentiodynamic polarization and electrochemical impedance spectroscopy (EIS) tests. The polarization data (Fig. 12a) were subsequently analyzed using Tafel extrapolation, with the corresponding fitting results presented in Table 1. As illustrated in the Fig. 12a, following the in-situ formation of the Mg-Al LDH coating, the corrosion potential was elevated, and the corrosion current density was reduced by approximately two orders of magnitude relative to the uncoated substrate. This substantial enhancement in corrosion resistance can be attributed to the compact microstructure of the LDH layer and the exchange of NO_3^- ions with the corrosive Cl^- species. Upon further modification with PFOTES, the composite coating exhibited pronounced superhydrophobicity, dramatically minimizing the interaction between the corrosive media (e.g., Cl^- ions) and the substrate surface. The corrosion potential was increased to −1.319 V, and the corrosion current density was reduced by an impressive three orders of magnitude compared to the bare substrate.

It is widely acknowledged that a high impedance modulus ($|Z|_{0.01\ Hz}$) in the low-frequency region and an elevated phase angle in the high-frequency region serve as hallmarks of supe-

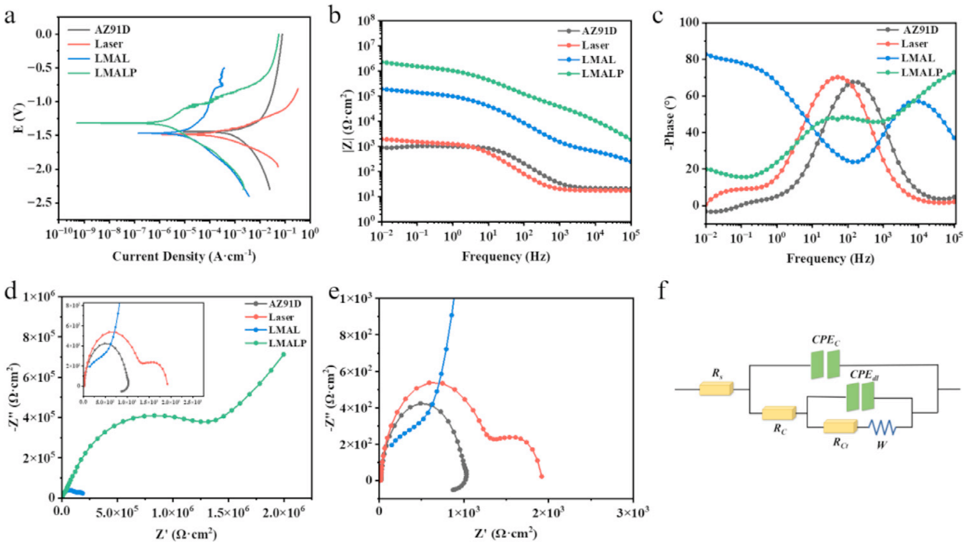

Fig. 12. (a) Polarization curves and EIS results of different samples in 3.5 wt.% NaCl solution: (b) Impedance-frequency Bode plots. (c) Phase-frequency Bode plots. (d) Nyquist plots and (e) Local magnification of Nyquist plots. (f) Equivalent electric circuit of LMALP.

rior corrosion resistance. Fig. 12b depicts the $|Z|_{0.01\ \mathrm{Hz}}$ values for all samples. For the LMAL coating, the observed improvement in corrosion resistance can be attributed to the synergistic effects of the LDH layer's robust physical barrier and active ion-exchange capabilities, resulting in an impedance value of 1.9×10^5 Ω·cm^2. In contrast, the composite LMALP coating demonstrated a substantially higher impedance, reaching 2.3×10^6 Ω·cm^2, owing to its hydrophobic properties. Among the tested samples, the LMALP composite coating exhibited the highest impedance modulus, underscoring its exceptional corrosion resistance. Moreover, the phase angle in the high-frequency region of the Bode plot is a pivotal parameter for evaluating corrosion resistance. As illustrated in Fig. 12c, the LMALP composite coating exhibited the largest phase angle in the high-frequency range, accompanied by a broad plateau. This observation suggests that the penetration of corrosive ions into the interface between the coating and the substrate was significantly impeded.

Nyquist plots presented in Fig. 12d and e further elucidate the variations in corrosion performance among the coatings. Typically, a larger capacitive arc diameter in the Nyquist plot is indicative of enhanced corrosion resistance. The capacitive arc diameter of the LMALP coating was significantly greater than that of other samples. Specifically, the incorporation of the LDH layer increased the capacitive arc diameter by approximately two orders of magnitude compared to the bare magnesium alloy substrate. Furthermore, the LMALP coating outperformed the LMAL coating, exhibiting a capacitive arc diameter roughly one order of magnitude larger. The remarkable improvement in corrosion resistance can be ascribed to the synergistic protection mechanisms of the LMALP composite coating. First, the LDH layer serves as a robust and impermeable physical barrier, effectively obstructing the infiltration of corrosive ions into the substrate. Second, the superhydrophobic nature of the LMALP surface, derived from its hierarchical micro-nanostructure, plays a critical role. According to the Cassie-Baxter theoretical model [45], air trapped within the surface microstructures drastically reduces the contact area between the solid surface and the corrosive liquid. This air layer significantly diminishes ion exchange and subsequent corrosion reactions, thereby markedly enhancing the protective efficacy of the coating.

Fig. 12f presents the simulated equivalent circuit for the LMALP coating. In this model, R_s and R_{ct} represent the solution resistance and charge transfer resistance, respectively, while the constant phase element (CPE) is used to represent the double-layer capacitance (CPE_c). In the simulation circuit, the coating is represented by R_c, and CPE_{dl} denotes the capacitance of the coating. The ion exchange occurring within the LDH intermediate layer induces diffusion, which is modeled using the Warburg diffusion element (W). Generally, a larger R_{ct} value correlates with improved corrosion resistance of the coating. According to the fitting data presented in Table 2, the enhanced R_{ct} value is attributed to the blocking effect of the LDH surface on certain corrosive ions and the ion exchange occurring within the interlayer. After modification with PFOTES, the R_{ct} value increased to 3.53×10^5 Ω·cm^2. This increase in R_{ct} is consistent with the radius of the capacitive arc observed in the Nyquist plots.

3.7. Self-healing property

To further investigate the long-term corrosion resistance of the composite coating, EIS was conducted on samples immersed in 3.5 wt.% NaCl solution for 0, 1, 4, 8, 12, and 16 days, as shown in Fig. 13. During the initial 1-day immersion, the impedance arc radius of the coating decreases significantly due to the corrosion of the composite coating by corrosive ions, resulting in a rapid decline in corrosion resistance. As the immersion time increases, the PFOTES layer gradually deteriorates, leading to a further decrease in the corrosion resistance of the composite coating, as indicated by

Table 2
Fitting results of EIS tests of different samples immersed in 3.5 wt.% NaCl solution for 30 min.

Sample	R_s ($\Omega\cdot cm^2$)	R_c ($\Omega\cdot cm^2$)	CPE_c		R_{ct} ($\Omega\cdot cm^2$)	CPE_{dl}		R_L ($\Omega\cdot cm^2$)	L ($H\cdot cm^2$)	W ($\Omega^{-0.5}\cdot S^{-1}\cdot cm^2$)
			Y_0 ($\Omega^{-1}cm^2s^n$)	n		Y_0 ($\Omega^{-1}cm^2s^n$)	n			
AZ91D	20.69	–	–	–	988	1.28×10^{-5}	0.92	6388	4.06×10^4	–
Laser	16.53	–	–	–	1288	1.51×10^{-5}	0.86	9156	5.13×10^4	–
LMAL	13.28	1354	6.19×10^{-8}	0.59	1.44×10^4	1.02×10^{-7}	0.98	–	–	7.62×10^{-5}
LMALP	10.00	3.52×10^4	9.38×10^{-9}	0.82	3.53×10^5	1.30×10^{-7}	0.62	–	–	3.39×10^{-6}

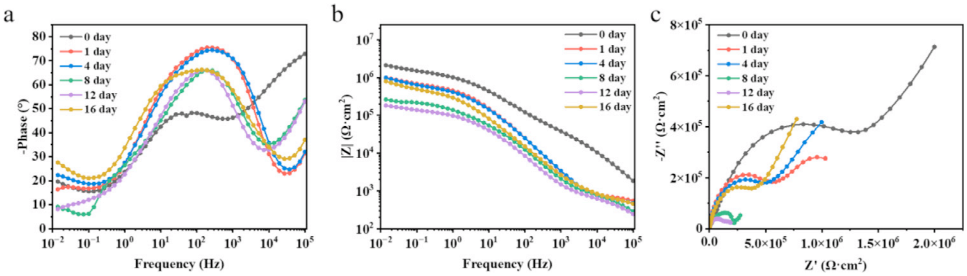

Fig. 13. Self-healing properties of LMALP: (a, b) Bode plots and (c) Nyquist plots.

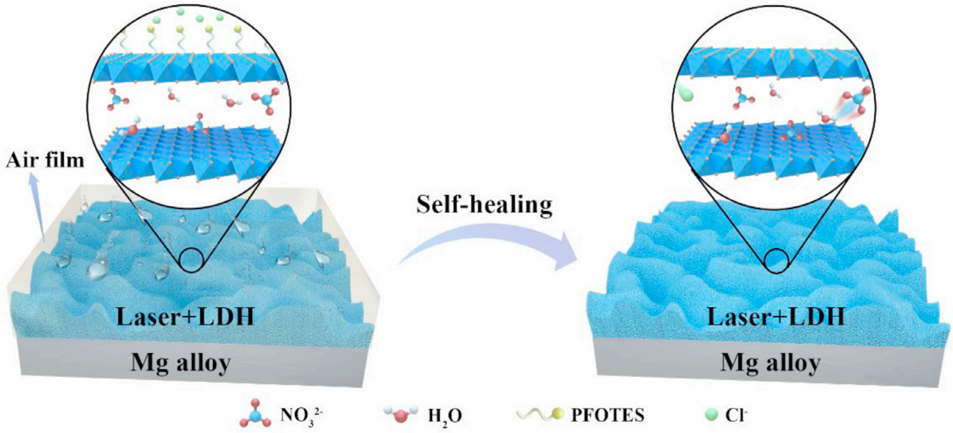

Fig. 14. The protection mechanism of bionic surface.

the progressive reduction in the impedance arc radius. At 8–12 days, the PFOTES layer completely fails, as evidenced by the decrease in low-frequency impedance modulus, with the 12-day measurement showing the lowest impedance values. However, between 12 and 16 days, an improvement in corrosion resistance was observed, with the impedance arc radius increasing. This unexpected enhancement can be attributed to the ion exchange between Cl^- and NO_3^- ions during the self-healing process of the LDH layer [48], which effectively slows down further corrosion progression despite the complete failure of the original PFOTES coating.

The protective mechanism of the biomimetic superhydrophobic coating can be described by two primary aspects. As shown in Fig. 14, firstly, PFOTES is incorporated as a surface modifier into the coating. Through hydrolysis and condensation reactions of PFOTES, the generated $CF_3(CF_2)_5(CH_2)Si(O^-)_3$ bonds with the Mg-Al LDH film. The C-F bonds exhibit strong chemical inertness, and the resulting molecular layer demonstrates a low surface energy, which significantly reduces the attraction between the surface and other molecules. This reduction in adhesion prevents the accumulation of contaminants, such as dust, and hinders the interaction between corrosive ions or molecular oxygen and the LDH film. Additionally, inspired by the micro-nanostructured surface of the centipede’s body, which exhibits low surface adhesion and enhanced contamination resistance, the superhydrophobic surface traps a substantial amount of air within its hierarchical micro/nanostructures, forming an air layer that acts as a physical barrier. This effectively isolates the corrosive medium from the substrate, thereby endowing the LMALP coating with exceptional barrier properties, reduced contaminant adhesion, and self-cleaning capabilities.

Secondly, when the composite coating is immersed in NaCl solution for an extended period, the continuous erosion by Cl^- ions leads to the failure of the fluorosilane layer, resulting in a reduction of the coating's hydrophobicity. This increases the contact area between the NaCl solution and the coating, allowing the corrosive media to come into contact with the Mg-Al LDH. However, the LDH coating formed on the magnesium alloy surface is dense and intact, effectively blocking the penetration of corrosion ions and prolonging the path for their movement. Additionally, the ion-exchange capacity of the LDH enables it to capture Cl^- ions, providing long-term protection for the magnesium alloy substrate.

4. Conclusion

In this study, a bioinspired centipede -like multi-level structured composite coating is successfully fabricated on the surface of magnesium alloy to improve its performance in marine environments. The main conclusions are summarized as follows.

(1) The composite coatings with bioinspired centipede-like structure created by femtosecond pulse laser and in-situ grown dense Mg-Al LDH nanosheets, form a complex micro-/nano-scale morphology, and provede a layer of air film. This is beneficial to achieving superhydrophobicity with a contact angle of 154.60°.
(2) The composite coatings demonstrated exceptional corrosion resistance with a reduction in corrosion current density by approximately five orders of magnitude compared to the bare magnesium alloy substrate, owing to the synergistic protective effects of dense Mg-Al LDH nanosheets and the air film. Firstly, the air film acts as a barrier against the corrosive media infiltration, secondly the LDH nanosheets captured Cl^- ions within the interlayer channels, and delaying the ion exchange of corrosive reactions.
(3) Under extreme conditions at -40 °C, the ice forming time on the coated surface is extended by 250% compared to the bare magnesium alloy, which highlighting its potential for applications in cold environments where delayed icing is crucial.
(4) The superhydrophobic coating simulates the macroscopic surface of the centipede and has excellent self-cleaning, anti-fouling, and mechanical durability properties. It performs effectively in dye immersion and dust contamination experiments and retained its superhydrophobicity after 7 cycles of sandpaper abrasion and 8 tape-peeling tests.

Overall, the bioinspired multiscale structured superhydrophobic coating demonstrated outstanding protective and functional properties, presenting significant potential for practical applications in the protection of magnesium alloys, especially in harsh marine environments.

Declaration of competing interest

The authors declare that they have no conflicts of interest to this work. We declare that we have no financial and personal relationships with other people or organizations that can inappropriately influence our work, there is no professional or other personal interest of any nature or kind in any product, service and/or company that could be construed as influencing the position presented in, or the review of, the manuscript entitled. Hongzhi Cui is an editorial board member for Journal of Magnesium and Alloys and was not involved in the editorial review or the decision to publish this article. All authors declare that there are no competing interests.

CRediT authorship contribution statement

Lin Dai: Writing – original draft, Methodology, Investigation, Data curation, Conceptualization. **Hongzhi Cui:** Writing – review & editing, Supervision, Project administration, Funding acquisition. **Xiaohua Chen:** Methodology, Investigation. **Ruiqi Xu:** Methodology, Investigation. **Yuhao Zhang:** Methodology, Investigation. **Leigang Li:** Writing – review & editing.

Acknowledgments

This research was supported by the National Natural Science Foundation of China (No. 52331004, U2106216), the Natural Science Foundation of Shandong Province (No. ZR2022ZD12), the Key R&D Program of Shandong Province, China (2023ZLGX05, 2023CXGC010406), Key Program of Natural Science Foundation of Shandong Province of China (No. ZR2022ZD12, ZR2024ZD14) and the Taishan Scholarship of Climbing Plan (No. tspd20230603).

Supplementary materials

Supplementary material associated with this article can be found, in the online version, at doi:10.1016/j.jma.2025.04.012.

References

[1] W. Yan, S. Xue, X. Zhao, W. Zhang, J. Li, Chin. Chem. Lett. 35 (2024) 109224.
[2] J. Bai, Y. Yang, C. Wen, J. Chen, G. Zhou, B. Jiang, X. Peng, F. Pan, J. Magnes. Alloys. 11 (2023) 3609–3619.
[3] X. Chen, J. Zhang, M. Wang, W. Wang, D. Zhao, H. Huang, Q. Zhao, X. Xu, H. Zhang, G. Huang, J. Magnes. Alloys. 12 (2024) 2147–2181.
[4] Q. Jiang, D. Lu, L. Cheng, N. Liu, L. Yang, B. Hou, npj Mater, Degrad 6 (2022) 28.
[5] Y. Ouyang, L.-X. Li, Z.-H. Xie, L. Tang, F. Wang, C.-J. Zhong, J. Magnes. Alloys. 10 (2022) 836–849.
[6] W. Yao, W. Liang, G. Huang, B. Jiang, A. Atrens, F. Pan, J. Mater. Sci. Technol. 52 (2020) 100–118.
[7] J. Xu, Q. Cai, Z. Lian, Z. Yu, W. Ren, H. Yu, J. Bionic Eng. 18 (2021) 735–763.
[8] Z.-Z. Yin, W.-C. Qi, R.-C. Zeng, X.-B. Chen, C.-D. Gu, S.-K. Guan, Y.-F. Zheng, J. Magnes. Alloys. 8 (2020) 42–65.

[9] X. Zhang, R. Li, X. Feng, X. Pang, X. He, Z. Jin, H. Ren, D. Wang, K. Li, X. Dai, Z. Du, Q. Zhou, Y. Zhang, J. Magnes. Alloys. 11 (2023) 1083–1093.

[10] X. Liu, T.C. Zhang, Y. Zhang, J. Rao, S. Yuan, J. Magnes. Alloys. 10 (2022) 3082–3099.

[11] S. Sun, P. Zhou, Y. Chen, J. Xiao, J. Sun, Y. Yuan, T. Zhang, F. Wang, J. Magnes. Alloys. 13 (2025) 207–218.

[12] D. Zhang, F. Peng, J. Qiu, J. Tan, X. Zhang, S. Chen, S. Qian, X. Liu, Corros. Sci. 192 (2021) 109840.

[13] Y. Zhang, N. Li, N. Ling, J. Zhang, L. Wang, Chem. Eng. J. 449 (2022) 137778.

[14] M. Yeganeh, N. Mohammadi, J. Magnes. Alloys. 6 (2018) 59–70.

[15] B.-Y. Liu, J. Wu, C.-H. Xue, Y. Zeng, J. Liang, S. Zhang, M. Liu, C.-Q. Ma, Z. Wang, G. Tao, Adv. Mater. 36 (2024) 2400745.

[16] X. Wang, C. Jing, Y. Chen, X. Wang, G. Zhao, X. Zhang, L. Wu, X. Liu, B. Dong, Y. Zhang, J. Magnes. Alloys. 8 (2020) 291–300.

[17] M.R. Hossain, R. Sultana, M.M. Patwary, N. Khunga, P. Sharma, S.J. Shaker, Environ. Chem. Lett 20 (2022) 1265–1273.

[18] X. Li, Z. Xue, W. Sun, J. Chu, Q. Wang, L. Tong, K. Wang, Chem. Eng. J. 454 (2023) 140187.

[19] C.-B. Li, F. Wang, R.-Y. Sun, W.-C. Nie, F. Song, Y.-Z. Wang, Chem. Eng. J. 450 (2022) 138031.

[20] Z. He, C. Wu, M. Hua, S. Wu, D. Wu, X. Zhu, J. Wang, X. He, Matter. 2 (2020) 723–734.

[21] D. Zang, R. Zhu, W. Zhang, X. Yu, L. Lin, X. Guo, M. Liu, L. Jiang, Adv. Funct. Mater. 27 (2017) 1605446.

[22] G.D. Bixler, B. Bhushan, Nanoscale 5 (2013) 7685–7710.

[23] Q. Sun, D. Wang, Y. Li, J. Zhang, S. Ye, J. Cui, L. Chen, Z. Wang, H.-J. Butt, D. Vollmer, X. Deng, Nat. Mater. 18 (2019) 936–941.

[24] D. Wang, Q. Sun, M.J. Hokkanen, C. Zhang, F.-Y. Lin, Q. Liu, S.-P. Zhu, T. Zhou, Q. Chang, B. He, Q. Zhou, L. Chen, Z. Wang, R.H.A. Ras, X. Deng, Nature 582 (2020) 55–59.

[25] K. Yin, L. Wang, Q. Deng, Q. Huang, J. Jiang, G. Li, J. He, Nano-Micro Lett 14 (2022) 97.

[26] Y. Liu, M. Wu, Z. Zhang, J. Lu, K. Xu, H. Zhu, Y. Wu, B. Wang, W. Lei, J. Mater. Sci. 58 (2023) 3421–3459.

[27] X. Jiang, C. Zhou, J. Su, S. Tang, Chem. Eng. J. 498 (2024) 155264.

[28] M. Zhou, L. Zhang, L. Zhong, M. Chen, L. Zhu, T. Zhang, X. Han, Y. Hou, Y. Zheng, Adv. Mater. 36 (2023) 2305322.

[29] R. Pan, H. Zhang, M. Zhong, ACS Appl. Mater. Interfaces. 13 (2020) 1743–1753.

[30] X. Feng, J. Chu, G. Tian, Z. Wang, W. Zhou, X. Zhang, Z. Lian, ACS Appl. Mater. Interfaces. 15 (2023) 53159–53171.

[31] H. Wang, Y. Song, X. Chen, G. Tong, L. Zhang, Corros. Sci. 208 (2022) 110699.

[32] A. Jagtap, P.G. Wagle, E. Jagtiani, A.P. More, J. Coat. Technol. Res. 19 (2022) 1009–1032.

[33] Y. Cao, D. Zheng, J. Luo, F. Zhang, C. Wang, S. Dong, Y. Ma, Z. Liang, C. Lin, Corros. Sci. 164 (2020) 108340.

[34] Y. Wu, L. Wu, M.L. Zheludkevich, Y. Chen, M. Serdechnova, W. Yao, C. Blawert, A. Atrens, F. Pan, J. Mater. Sci. Technol. 91 (2021) 28–39.

[35] T. Shulha, M. Serdechnova, T. Wu, T. Naacke, G. Wiese, C. Blawert, M.L. Zheludkevich, Nano Mater. Sci. 6 (2024) 428–442.

[36] Q. Li, X. Zhang, S. Ben, Z. Zhao, Y. Ning, K. Liu, L. Jiang, Nano Res 16 (2022) 3312–3319.

[37] B. Pillado, B. Mingo, R. del Olmo, E. Matykina, A.M. Kooijman, Y. Gonzalez−Garcia, R. Arrabal, M. Mohedano, J. Magnes. Alloys. 11 (2023) 201–216.

[38] L. Wu, J. Wu, Z. Zhang, C. Zhang, Y. Zhang, A. Tang, L. Li, G. Zhang, Z. Zheng, A. Atrens, F. Pan, Appl. Surf. Sci. 487 (2019) 569–580.

[39] Y. Xia, W. Gu, Q. Zhang, Z. Yang, X. Lv, Y. Ji, W. Deng, W. Liu, L. Dong, P. Feng, Q. Ran, X. Yu, Y. Zhang, Adv. Funct. Mater. (2024) 2412379 n/a.

[40] S. Wu, J. Huang, J. Fang, D. Li, J. Lu, L. Xiang, N. Dai, Y. Zhang, Y. Xiao, W. Xiong, Surf. Coat. Technol. 470 (2023) 129870.

[41] J.-M. Wang, X. Sun, L. Song, M.B. Kannan, F. Zhang, L.-Y. Cui, Y.-H. Zou, S.-Q. Li, R.-C. Zeng, J. Magnes. Alloys. 11 (2023) 2967–2979.

[42] N. Huang, Y. Wang, Y. Zhang, L. Liu, N. Yuan, J. Ding, Surf. Coat. Technol. 463 (2023) 129539.

[43] Y. Wang, X. Zhou, M. Yin, J. Pu, N. Yuan, J. Ding, Langmuir 37 (2021) 8129–8138.

[44] K.V. Nadaraia, S.N. Suchkov, I.M. Imshinetskiy, D.V. Mashtalyar, D.Y. Kosianov, E.A. Belov, S.L. Sinebryukhov, S.V. Gnedenkov, J. Magnes. Alloys. 11 (2023) 1721–1739.

[45] Z. Xin, C. Zhang, Z. Wei, L. Wang, Y. Lu, Chem. Eng. J. 490 (2024) 151334.

[46] Z. Wang, Y. Hou, A. Yadav, T. Chen, Y. Wu, C. Yan, M. Liu, ACS Appl. Mater. Interfaces. 17 (2025) 7174–7189.

[47] Y. Guo, H. Zhao, C. Zhang, G. Zhao, Chem. Eng. J. 497 (2024) 154383.

[48] A.S. Gnedenkov, S.L. Sinebryukhov, A.D. Nomerovskii, V.S. Filonina, A.Y. Ustinov, S.V. Gnedenkov, J. Magnes. Alloys. 11 (2023) 3688–3709.